Orbital microwave measurement of river discharge and ice status

G. Robert Brakenridge,[1] Son V. Nghiem,[2] Elaine Anderson,[1] and Rodica Mic[3]

Received 8 June 2006; revised 20 September 2006; accepted 15 November 2006; published 4 April 2007.

[1] Satellite passive microwave sensors provide global coverage of the Earth's land surface on a near-daily basis without severe interference from cloud cover. Using a strategy first developed for wide-area optical sensors, and in conjunction with even limited ground-based discharge information, such microwave data can be used to estimate river discharge changes, river ice status, and watershed runoff. Water surface area in a river reach increases as flow widens, and any temporally calibrated observation sensitive to changing water area monitors discharge. The sensor spatial resolution is less important than the scene-to-scene calibration and the contrast in upwelling radiance between water and land. We use the Advanced Microwave Scanning Radiometer (AMSR-E) band at 36.5 GHz, descending orbit, horizontal polarization, and the resampled Level-3 daily global data product. The discharge estimator *HR* is a ratio of calibration-target radiance (expressed as brightness temperature), for a local land parcel unaffected by the river, to measurement-target brightness temperature, for a pixel centered over the river. At midlatitudes, pixel dimensions are approximately 25 km. Because of low emission from water surfaces, *HR* increases with discharge as in-pixel water area expands. It increases sharply once overbank flow conditions occur. River ice-cover is also detectable. The sensitivity and accuracy of the orbital measurements is tested along U.S. rivers monitored by in situ gaging stations, with favorable results. Other tests demonstrate that for seasonally variable rivers, AMSR-E can provide useful international measurements of daily river discharge even if only fragmentary monthly mean discharge data are available for calibration.

Citation: Brakenridge, G. R., S. V. Nghiem, E. Anderson, and R. Mic (2007), Orbital microwave measurement of river discharge and ice status, *Water Resour. Res.*, *43*, W04405, doi:10.1029/2006WR005238.

1. Introduction

[2] Previous research [*Smith*, 1997; *Smith et al.*, 1996, 1995] demonstrates that orbital sensors can measure discharge changes along braided rivers. Imaging of surface water area in a river reach provides a proxy indicator of discharge that can be nearly as robust as stage-based (water level) discharge estimation [*Ashmore and Sauks*, 2006]. Each technique has advantages and limitations. In situ stage measurement [*Rantz et al.*, 1982] can be continuous and very precise (water level to a few centimeters). Along some reaches, in-channel flow variation occurs with little width change, and stage monitoring is the best approach. In contrast, remote sensing is applicable to river reaches where flow area changes are significant and consistent over time. The available satellite technology of wide-swath sensors can provide daily or near-daily measurements. Remote sensing is economical; it observes rivers regardless of international borders, and it can uniquely contribute direct measurements of floodplain inundation [*Brakenridge et al.*, 2005]. We test here the use of wide-swath passive microwave satellite data that resample rivers at the same wavelength, polarization, and time-of-day and as frequently as once every 1–2 days. To obtain the most useful results, such remote sensing data require calibration to discharge by comparison to some in situ discharge measurements. Empirical rating curves can thereby be constructed and periodically updated, using the same approach that has long been used for station-based discharge measurements.

[3] A possible limitation of using water surface area for estimation of discharge is the relatively small spatial scale of river width and associated reach surface water area changes [*Bjerklie et al.*, 2003]. Significant in-channel discharge changes along some rivers may produce river width changes of only a few meters. Frequent-repeat sensors, which are needed for an adequate temporal resolution, commonly do not provide the spatial resolution needed to measure such changes. However, as is the case for stage-gaging sites [*Wahl et al.*, 1995], measurement locations can be chosen to maximize measurement sensitivity and reliability. When water area changes over kilometers of a river reach are measured, instead of at-a-section width, then the observational precision requirements can be met. Also, most river reaches include tributary stream junctions, slip-off slopes across the inside bends of meandering rivers, channel bars and islands, and other features which are sensitive to relatively small discharge changes. The presence of such

[1] Dartmouth Flood Observatory, Department of Geography, Dartmouth College, Hanover, New Hampshire, USA.
[2] Jet Propulsion Laboratory, California Institute of Technology, Pasadena, California, USA.
[3] National Institute of Hydrology and Water Management, Bucharest, Romania.

0043-1397/07/2006WR005238$09.00

Table 1. AMSR-E Radiometer Characteristics

	Center Frequencies, GHz					
	6.92	10.65	18.7	23.8	36.5	89
Sensitivity, K	0.3	0.6	0.6	0.6	0.6	1.1
Instantaneous field of view, km	76 × 44	49 × 28	28 × 16	31 × 18	14 × 8	6 × 4
Sample spacing, km	10 × 10	10 × 10	10 × 10	10 × 10	10 × 10	5 × 5

features can lead to significant aggregate increases in reach water surface area as the river rises, even if overbank conditions are not attained [*Brakenridge et al.*, 2002]. In this regard, a reach measurement approach is fundamentally different than a cross-section measurement approach: It makes use of the spatially continuous coverage provided by imaging remote sensing.

[4] The Advanced Microwave Scanning Radiometer–Earth Observing System (AMSR-E on NASA's Aqua satellite) provides frequent global coverage for the Earth's surface and, at 36.5 GHz, without severe interference from clouds. This paper demonstrates that by using a strategy first developed for wide-area optical sensors [*Brakenridge et al.*, 2005, 2002], AMSR-E can measure river discharge changes and river ice status. Because the sensor provides data at a variety of frequencies, polarizations, look angles, and time-of-days, we first consider which of these data are most appropriate for consistent responses to changing water surface areas. Then the remote sensing data are presented for two U.S. river reaches that are colocated to ground-based gaging stations. This allows an examination of the remote sensing signal response to known daily discharge changes. Similar measurements are then analyzed for rivers in Europe, Asia, and Africa, where published discharge data are limited but where it is still possible to obtain reliable calibrations of the remote sensing signal using a comparison of monthly means. Finally, we demonstrate that AMSR-E data can also indicate the timing of ice-covered and ice-free conditions in cold region rivers.

2. Selection of AMSR-E Data

[5] AMSR-E operates in a polar Sun-synchronous orbit at 98.2° inclination with ascending equator crossings at 1330 LT. The imaged swath width is 1445 km, providing full global coverage within 3 days. This radiometer has six frequencies (Table 1) measuring radiances on a brightness temperature scale, and at an incidence angle of 54.8° on the Earth's surface.

[6] The low-frequency channels at 6.92 and 10.65 GHz have very coarse resolutions and suffer from radio frequency interferences [*Njoku et al.*, 2005]. The resolutions of 18.7- and 23.8-GHz channels are coarse, and these channels are close to the water vapor spectral line [*Skou*, 1989]; thus they are susceptible to atmospheric conditions. The 89.0-GHz channel has the best resolution of 6 × 4 km; however, it is close to the oxygen spectral line [*Skou*, 1989] and may contain large atmospheric contaminations. For our purpose, the 36.5-GHz channel appears to be optimal.

[7] AMSR-E signatures are sensitive to surface wetness [*Njoku et al.*, 2003]. The brightness temperature T_{bp} is related to the physical temperature T and surface emissivity e_p as

$$T_{bp} = T \cdot e_p \text{ for polarization } p = H, V, \tag{1}$$

where H represents the horizontal polarization and V is the vertical polarization. Emissivity conveys information related to surface wetness; however, the physical temperature is variable and can change significantly in different seasons. Thus a functional combination of data should be used to retain the best sensitivity to surface water while minimizing effects of variable physical temperature.

[8] We investigate passive microwave signature at 36.5 GHz and 54.8° incidence angle, consistent with the AMSR-E characteristics, to identify the best specific approach to measuring river discharge. We use an emission model developed under the fluctuation-dissipation theory [*Tsang*, 1991; *Tsang et al.*, 1985; *Yueh et al.*, 1992]. The dyadic Green's function used in the emission model is derived for heterogeneous geophysical media [*Nghiem et al.*, 1990]. For a silt-loam soil type [*Fairbridge and Finkl*, 1979] with 27% clay, 62% silt, and 11% sand at 298 K (25°C), the soil dielectric constant is given in Table 2 as a function of volumetric soil moisture [*Calvet et al.*, 1995].

[9] We have used the values of soil dielectric constant in Table 2 in the calculation of the traditional polarization ratio PR defined as [*Njoku et al.*, 2003]

$$PR = (T_{bV} - T_{bH})/(T_{bV} + T_{bH}). \tag{2}$$

Now we plan a different approach (the present "paired measurement method") that uses a ratio of a brightness-temperature pair defined for the horizontal and vertical polarizations, respectively, as

$$HR = T_{bH}(C)/T_{bH}(M), VR = T_{bV}(C)/T_{bV}(M), \tag{3}$$

where C denotes a calibration target area and M represents a measurement area in a river reach. Substituting (1) in (3), the pair ratio becomes

$$HR = [T(C)/T(M)] \cdot [e_H(C)/e_H(M)] \approx e_H(C)/e_H(M) \tag{4a}$$

$$VR = [T(C)/T(M)] \cdot [e_V(C)/e_V(M)] \approx e_V(C)/e_V(M). \tag{4b}$$

The approximation in (4a) and (4b) holds when $T(C) \approx T(M)$ signifying that the physical temperature is similar at C and M.

[10] The C and M pair is selected such that (1) C is located near M so that they are within the correlation length scale of physical temperature T and thus T is approximately cancelled in the paired ratio, (2) C and M are separated by a short distance so that measurements acquired by AMSR-E are effectively (a few minutes) contemporaneous, (3) C is at an area least affected by water change away from the local river reach M and thus C can be used as a relatively stable calibration target unaffected by the river change, and (4) M is selected such that its area contains the largest change in reach water surface area with discharge changes.

Table 2. Complex Dielectric Constant at 36.5 GHz of a Silt-Loam Soil at 25°C

	Volumetric Soil Moisture, %						
	5	10	15	20	25	30	35
Real part	3.76	4.41	5.57	6.81	7.78	8.73	9.69
Imaginary part	0.21	1.23	2.82	4.63	5.98	8.25	9.94

[11] As river discharge increases, local water tables rise, the fractional area of open water increases, and (if local precipitation is occurring) soil moisture may also increase preferentially along the floodplain lowlands [*Jung et al.*, 2004]. To investigate these effects, we increase volumetric moisture m_v between 10% and 35% and also water fraction f_w between 10% and 90% over M. We obtain the results for up to m_v = 35% approaching the limit of soil-moisture saturation while allowing the water fraction f_w to vary over a large range from 10% to 90%. The range of f_w depends on how M is chosen, and f_w can have the maximum value of 100% if M fully conforms to the flooded area.

[12] For the case of soil moisture change (Figure 1a), we change m_v over M to calculate HR and VR while keeping f_w = 10% in M and m_v = 5% in C. For the case of water fraction change (Figure 1b), we use the linear mixing of water and soil areas over M since the emissivities from these different areas are uncorrelated within the 14 × 8 km footprint at 36.5 GHz (8.2-mm wavelength). In this case, we consider m_v = 10% for a drier condition (thin curves in Figure 1b) and m_v = 20% for a wetter condition (bold curves in Figure 1b) over the soil area in M while keeping m_v = 5% in C. When rainfall occurs over both M and C due to their close proximity, soil moisture can increase in both areas while the reach water surface area increases in M. We analyze this case by starting from $f_w(M)$ = 10% and $m_v(M) = m_v(C)$ = 10% and linearly increasing the values to $f_w(M)$ = 90% and $m_v(M) = m_v(C)$ = 35% (medium thickness curves in Figure 1b). In all cases, the water dielectric constant at 36.5 GHz is (21.4 + i30.6) obtained from a published empirical function [*Klein and Swift*, 1977]. PR is also calculated over M using the same input parameters.

[13] The results indicate that HR has the best sensitivity in each case. Since effects of both increasing m_v and increasing f_w are directly related to HR (i.e., positive slopes in both cases), the combined effects of wetter soil and wider river also have the best sensitivity in HR compared with VR and compared with the traditional polarization ratio PR, which has the least sensitivity by an order of magnitude. Note that HR increases strongly as a function of river water fraction f_w for the different values of soil moisture representing drier and wetter conditions over the soil area, within the river reach measurement area M (Figure 1b).

[14] Thus HR increases as river rise commences, and then HR increases sharply once overbank flow conditions occur over a large part of M. These results suggest that M should be selected such that f_w is the largest for the maximum overflow condition to obtain the best sensitivity for river discharge measurement. Moreover, the model analysis

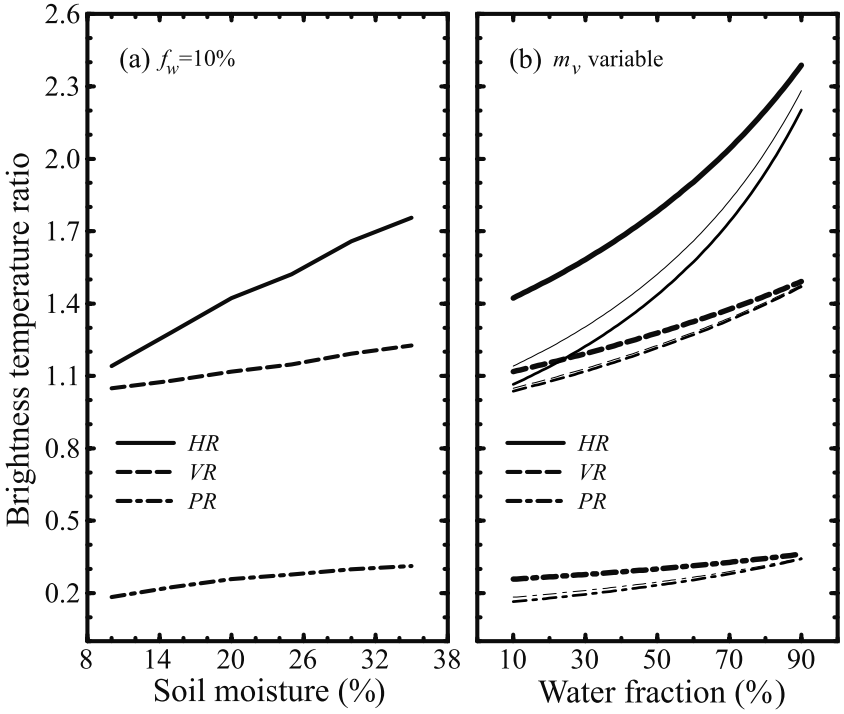

Figure 1. Change in brightness temperature ratios HR, VR, and PR at 36.5 GHz versus (a) soil moisture for f_w = 10% in the river reach M and m_v = 5% in C, and (b) water fraction for $m_v(M)$ = 10% and $m_v(C)$ = 5% represented by the thin black curves, for $m_v(M)$ = 20% and $m_v(C)$ = 5% by the bold black curves, and for m_v from 10% to 35% in both M and C by the curves with medium line thickness. Note that the dashed thin black curve and the dash-dotted thin black curve are very close to the corresponding medium-line curves plotted in the right panel.

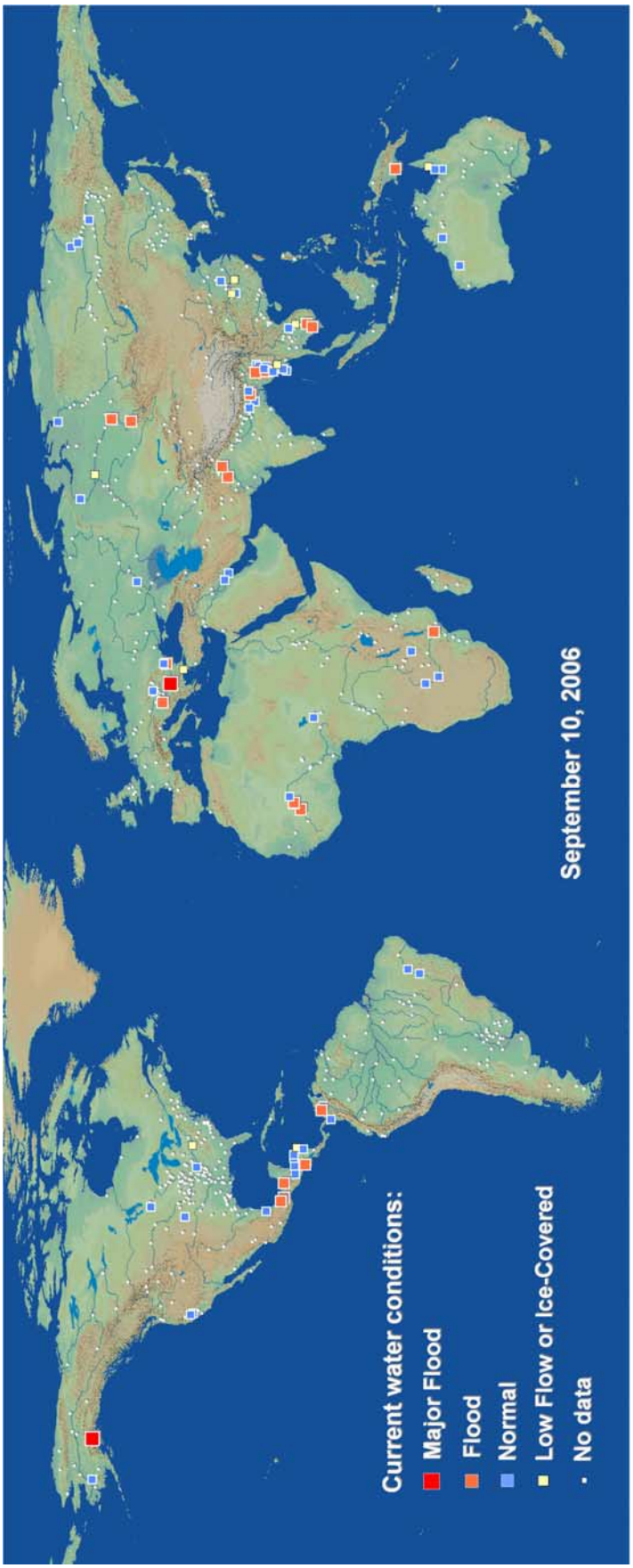

Figure 2. Display of 57 gaging reach locations and their daily discharge status, using a percentile approach applied to the AMSR-E period of record (since mid-2002). Estimated discharges exceeding the 95th percentile are classified as "major flood," between 80 and 95th percentile are classified as "flood," and from the 5th to 80th percentile are classified as "normal." Where *HR* indicates unusually little surface water, or where other criteria indicate ice-covered river conditions, the "low flow or ice-covered" symbol is displayed. Six hundred other measurement locations ("no data" symbol) have so far been identified.

shows an increasing trend of *HR* without a saturation effect as functions of both m_v and f_w (Figure 1), establishing the validity of the pair measurement method over a wide range of river flow variations. Another result from the model calculations is that the medium thickness curves for the case of soil moisture increase in both *M* and *C* (Figure 1b) stay closer to those of the drier condition (thin curves) with a smaller difference between $m_v(M)$ and $m_v(C)$ compared with those of the wetter condition in *M*, whereas *C* remains very dry (bold curves). This suggests that the pair ratio *HR* or *VR* reduces the effects of soil moisture change when both *C* and *M* becomes wetter or drier; therefore *C* and *M* should be chosen in a close proximity.

[15] Furthermore, the close proximity between *C* and *M* is important in reducing errors caused by uncorrelated changes in vegetation conditions, soil characteristics, and rainfall distribution. When *C* and *M* are sufficiently close, changes at these locations are more likely to be correlated, e.g., similar vegetation growth rate at *C* and *M*. In this case, the pair ratio approach accounts for the correlated changes that are inherently included in the rating relationship between the brightness temperature ratio and river gage data. Nevertheless, in cases of large variabilities between *C* and *M*, such as small but heavy rain cells in the tropics, the error can be large and thus limit the applicability of this method. Also, impervious surfaces and man-made hydrologic systems in urban areas significantly alter the natural stream flow response and can cause significant errors when urban areas occupy the majority of the surface in either *C* or *M*.

[16] The above calculations are for a bare surface without vegetation cover, atmospheric effects, and diurnal variability. With vegetation and atmospheric attenuations, the signature related to river discharge becomes weaker as it is partially masked. In this case, it is even more important to select the ratio with the best sensitivity to river discharge change, namely, *HR*. Because the attenuations can be strong in vegetated areas, we expect that *HR* is significantly lower than the model result, as high as 2.3 in Figure 1b, calculated for a bare surface as an upper bound.

[17] To retain the best sensitivity of *HR* to surface water, river reach areas *M* should be chosen so that discharge changes produce the largest water surface area changes. Such selection forces *HR* to the higher range of f_w corresponding to a steeper slope of the *HR* curve, and thus a higher sensitivity of *HR* to the water fraction (Figure 1b). In order to select reach areas *M* where flow area expansions occur, we use overbank flooded areas measured by the Moderate Resolution Imaging Spectroradiometer (MODIS) and other satellite sensors archived at the Dartmouth Flood Observatory (available in an online atlas; see *Brakenridge and Anderson* [2006b]).

3. Gaging Reach Locations

[18] For the following, the specific AMSR-E data product used is the "AMSR-E/Aqua Daily L3 Surface Soil Moisture, Interpretive PARMS, and QC EASE-GRIDS V001" obtainable via the file transfer protocol (ftp) from the National Snow and Ice Data Center (NSIDC) in Boulder, Colorado. The temporal span of these data extends from June 2002 to the present, and the sampling is daily.

[19] Our purpose is to test a technique that can be generally applicable. To this end, a reach-based prototype global river discharge monitoring system ("Surface Water Watch," Figure 2) has been developed, and the ongoing results are posted online at http://www.dartmouth.edu/~floods/. Fifty-seven river reaches of approximately 25-km length were chosen where previous remote sensing at optical wavelengths (250-m spatial resolution) observed significant ($>\sim$20 km^2 per river reach) water area variations during 1999–2005. Approximately 600 other locations, globally, meet these initial selection criteria, but data have not yet been collected and analyzed (Figure 2). Close to each of the measurement reach pixels (*M*) within the AMSR-E data product, a calibration target pixel (*C*, unaffected by the river or stream change) was also selected. Figure 3 provides locations of the measurement and calibration pixels for the reaches analyzed in this paper. Land cover at the reaches varies from row crop or other agriculture, to savannah, and forest. Some of the reaches are in regions affected by seasonal or permanent frozen ground and by snow. A variety of topographic settings occur, from nearly level terrain to rivers flowing within hilly upland terrains.

4. Results for U.S. Test Reaches

[20] The examples from within the United States are colocated to in situ gaging stations where daily discharge data are available. This makes possible the comparison of the *HR* daily measurements to discharge. As per the prior sections, we expect that (1) overbank flood discharges should be measurable, whereas some in-channel flow variation might not produce a sufficient variation in water surface area within such large (25 × 25 km) pixels to be detectable, and (2) *HR* values should range generally between $\sim$0.9 and 1.5 in response to reach water surface area changes.

[21] Also, we expect possible lag times between maximum flood discharge and maximum *HR* for particular events. This is because, depending on floodplain-channel interconnectivity [*Anderson et al.*, 1996; *Bates et al.*, 2002; *Bayley*, 1991], flood peaks measured at a gaging station may precede (several hours to perhaps several days) maximum inundation of the floodplain. In this regard, river flooding sometimes occurs via a combination of rising river stage, the emergence of shallow floodplain water tables, and direct precipitation on the saturated floodplain: Floodwater can have both local and upriver sources [*Mertes*, 1997]. Where channel water decanting overbank is the sole source, flooding is more likely to lag river stage rise; where local water is important in flooding from incoming local precipitation and/or snowmelt, inundation may occur nearly synchronously with rising local river stage.

[22] Figure 4 presents two discharge-*HR* relations plotted as scatterplots on arithmetic scales. No lag times are incorporated into either plot. In both cases, there is a correlation between measured discharge and *HR*, with least squares R^2 values from a fourth-order polynomial regression (1410 observations, July 2002 to April 2006) of 0.74 for the Red River and 0.63 for the Wabash (Figure 4). Also, the results are consistent with the expectation regarding the relative sensitivity of *HR* to low, in-channel, and overbank flow variation. Namely, (1) very low *HR* of 0.91–0.99 is always correlated to very low discharge, (2) intermediate ratios of 1.0–1.1 for the Red River and 1.0–1.04 for the

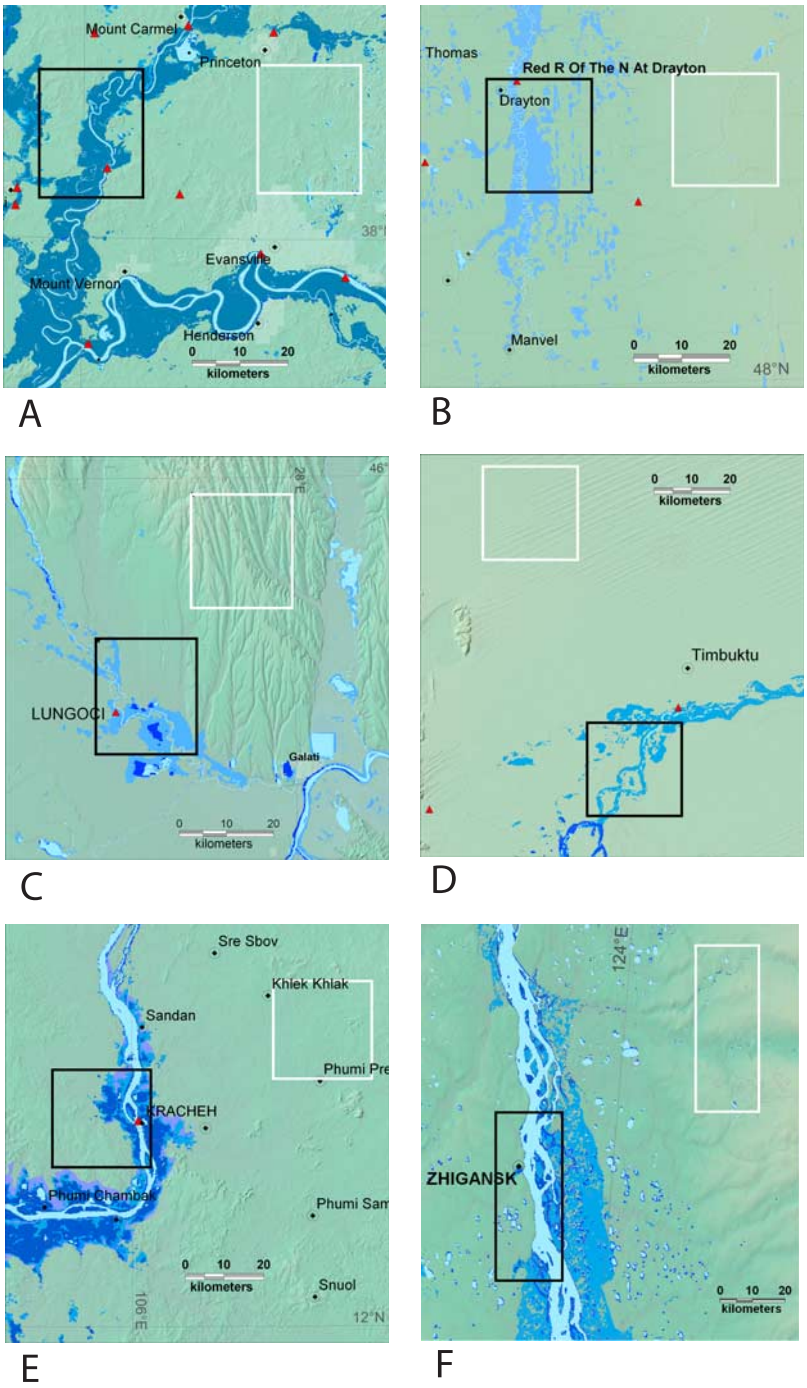

Figure 3. Location maps and remotely sensed surface water variability for six gaging reaches being monitored using AMSR-E data. NASA's Moderate Resolution Imaging Spectrometer (MODIS) images, classified to water/land products, provide in-channel flow (light blue) and maximum observed flood (darker blue) surface water extents. The black rectangles outline the measurement pixels, and the white rectangles outline the calibration pixels. Red triangles are locations of in situ gaging stations. (a) Reach 187, Wabash River near New Harmony, Indiana. (b) Reach 134, Red River of the North near Drayton, North Dakota. (c) Reach 268, Siret River near Galati, Romania. (d) Reach 433, Niger River near Timbuktu, Mali. (e) Reach 77, Mekong River near Krachech, Cambodia. (f) Reach 1, Lena River near Zhigansk, Russia. The rectangular pixel dimensions in the Lena example are actual land areas sampled due to the effects at high latitudes of using globally projected image data.

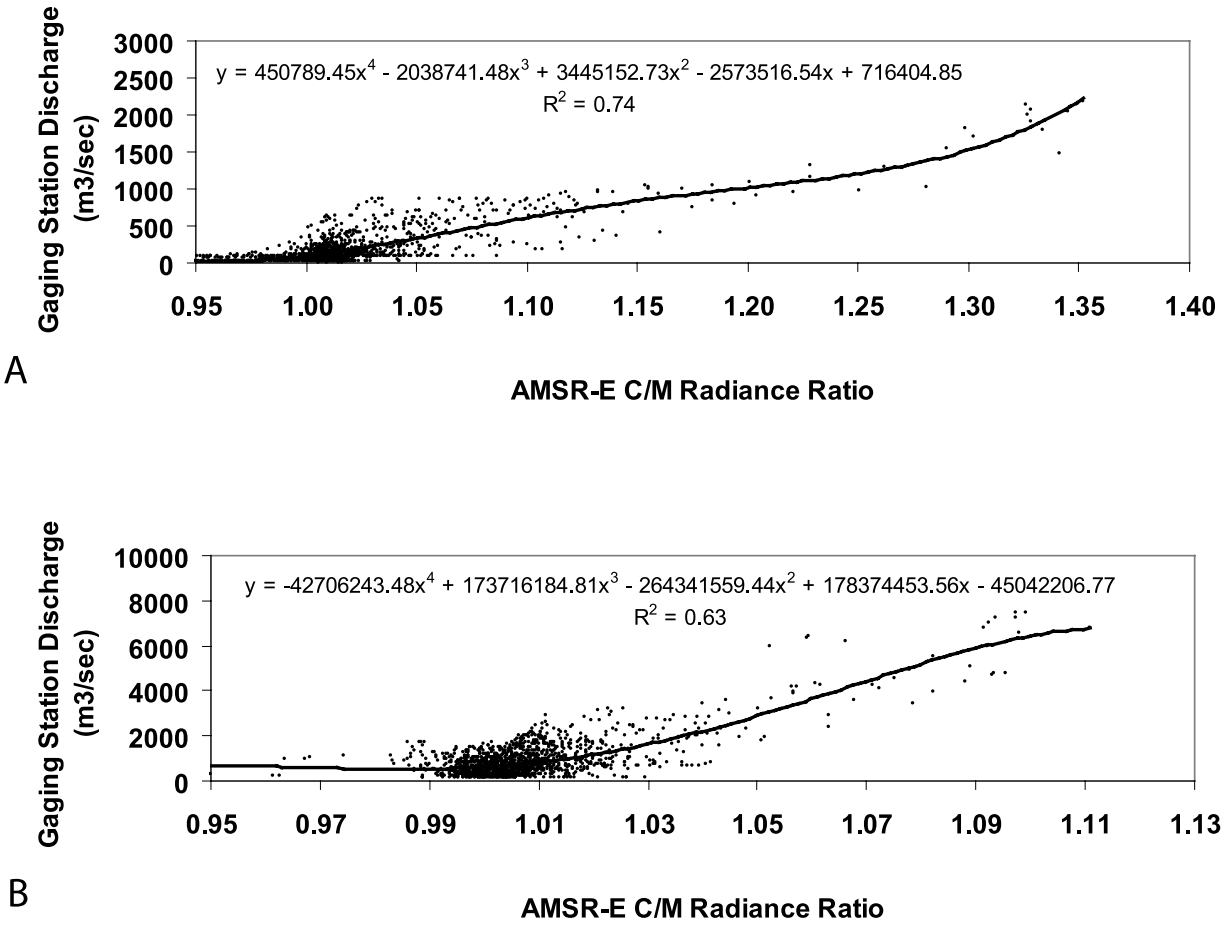

Figure 4. Scatterplots of AMSR-E C/M radiance ratios (*HR*) versus gaging station discharge for (top) the Red River near Drayton, North Dakota, and (bottom) the Wabash River near New Harmony, Indiana. See Figure 3 for reach and gaging station locations.

Wabash River are matched by low to moderate in-channel discharges, but with a relatively large scatter, and (3) for above-bankfull discharges along both rivers (>1000 m^3/s for the Red River and >2000 m^3/s for the Wabash River), scatter is reduced and the relations appear to be approximately linear: Higher ratios, >1.1 and >1.04, respectively, are correlated to progressively higher flood discharges for these two rivers.

[23] To consider further how *HR* responds to discharge, Figure 5 compares the gaged discharge as measured at the local stations to the remote sensing result through time. To facilitate this comparison, the estimated discharge obtained by application of the rating equations (Figure 4) is plotted together with discharge measured at the gaging stations. For the Red River, the times series is illustrated without any lag times, whereas for the Wabash River, a constant 2-day lag is added: by displaying the daily gaging station discharge 2 days after the actual dates. The comparisons in time further demonstrate the utility of this remote sensing technique for measuring discharge variation: Estimated discharge generally tracks actual discharge, and the flood events in particular are well characterized. Also, the plots demonstrate that along this reach of the Wabash River, lag times of approximately 2 days occur between peak gaging station discharge and peak *HR* values (and associated estimated discharge); whereas, for the Red River, remote sensing based flood hydrographs do not generally lag station-based flood hydrographs (compare the two time series in Figure 5).

[24] In regard to the lack of lag times for the Red River, this floodplain is within very flat (glacial lake bed) terrain where flooding is commonly induced by direct precipitation on the floodplain surface and, in the spring, by snowmelt. Thus we believe the gaged river height at Drayton rises nearly synchronously with inundated area and *HR*. In contrast, depending on the season and the spatial distribution of flood-producing precipitation within the watershed, the steeper-gradient Wabash River (Figure 3) may flood a drier floodplain, and inundated area expands as this channel-derived water fills, first the lowermost floodplain surfaces (for example, along crevasse splays) and then the higher floodplain and low terrace surfaces. In this case, small-scale topography, hydraulic connectivity, and local resistance to flow regulate the pattern and rate of inundation.

[25] A closer examination of the scatterplots and the times series for both rivers further characterizes the AMSR-E signal response to river hydrology. The Red River reach includes a sinuously meandering channel (Figure 3), with a bankfull discharge of approximately 1000 m^3/s flowing through a nearly level plain that is heavily utilized

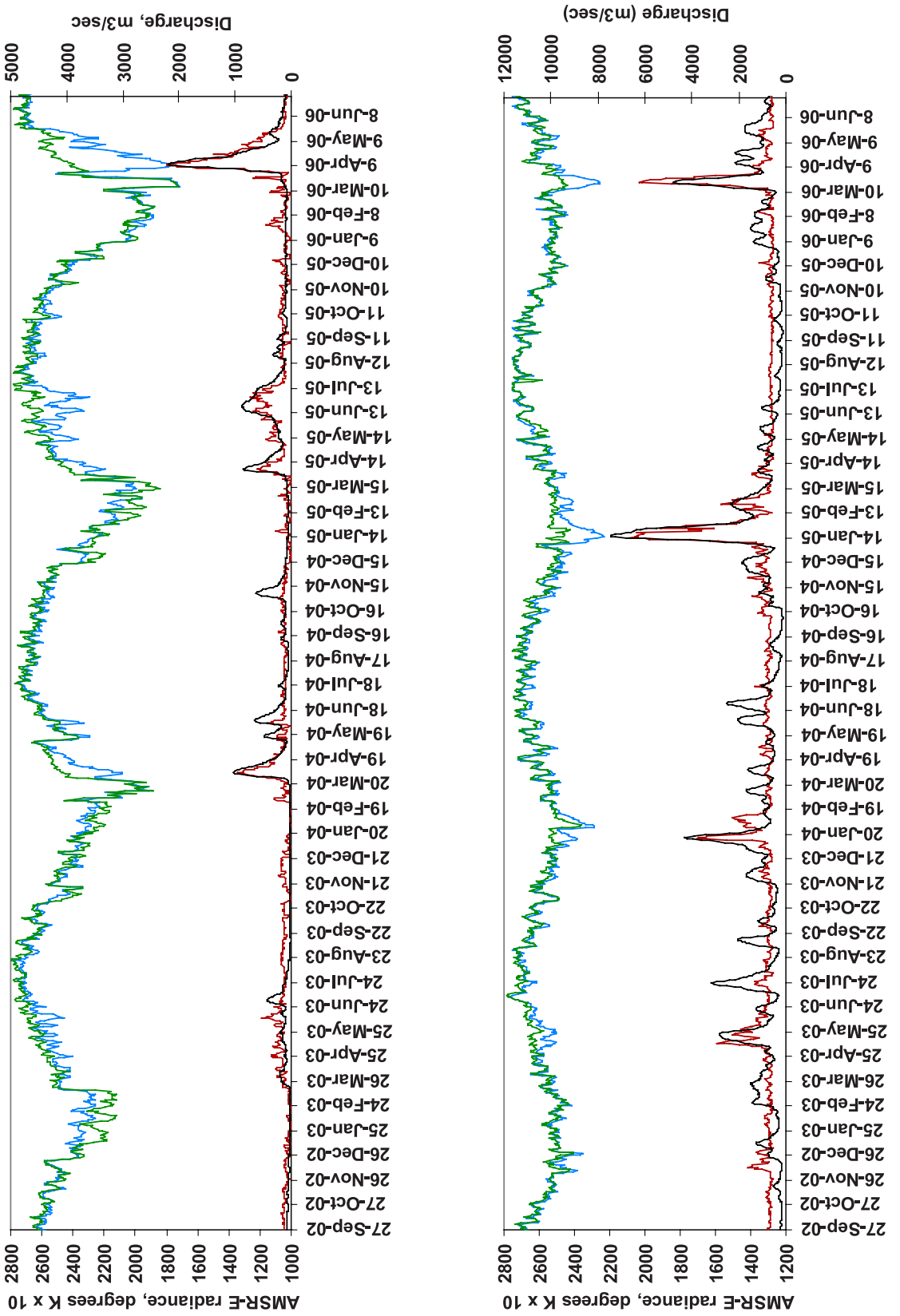

Figure 5. AMSR-E radiance data (left axis scale) for the measurement (blue line) and calibration (green line) pixels, (top) Red River near Drayton and (bottom) Wabash River near New Harmony, for mid-2002 to mid-2006. Also shown, using the right axis scale, are the local gaging station discharges (black line) and the remote sensing-based discharge estimates (brown line).

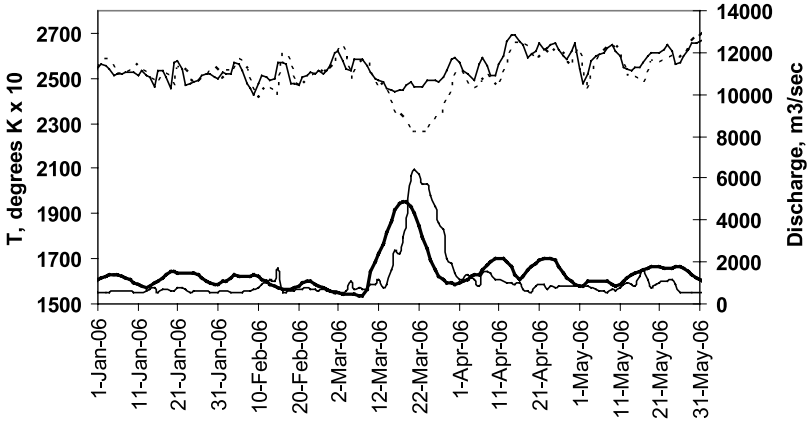

Figure 6. Flood in March 2006 along the Wabash River recorded by the gaging station (lower plot, bold black line) and by *HR* from AMSR-E data (lower plot, thin black line). In these expanded plots, no lag time is added to the gaging station record (a 2-day lag was incorporated in Figure 5 for the Wabash). Peak discharge was reached at the gaging station 2–3 days before peak discharge as inferred from the AMSR-E, and due to the local inundation dynamics. Also shown are the AMSR-E radiance data used to calculate *HR*: Dotted line shows radiances from the measurement pixel, and solid line shows that from the calibration pixel (these use the left axis scale).

for agriculture. The annual microwave brightness temperature range is approximately 60°K for both measurement and calibration pixels; snow cover, crop cover, urban extent, mean slope, and soil moisture also affect the brightness temperature/radiance values of both pixels (Figure 5). The direct impact of discharge changes on just the measurement pixel is illustrated in the plots (compare blue and green lines in Figure 5). Each overbank flood (five in the period of record) was recorded by AMSR-E data, and their relative amplitudes and durations are well characterized. However, more modest high flows, below bankfull, are not consistently matched by similar changes in *HR* or by drops in the measurement pixel brightness value (see late November flood of 2004; Figure 5). Finally, sustained periods of low flow are well characterized in time, but discharge estimates are not very accurate on a percent basis during these low flows.

[26] Also for the Red River, there occurs an apparent observation error for major flooding in June and July 2005. The gaging station recorded a prolonged but relatively steady interval of high discharge, whereas the sensor instead observed this flood as two discrete flood peaks (Figure 5). It is a temporary drop in the calculated discharge based on AMSR-E data centered about 26 June that introduces this error. An examination of the brightness temperature values indicates a sharp but short-lived rise at both pixels at this time. We infer that another, nonwater variable strongly affected the microwave returns from both pixels: This change was sufficient to alter the ratio (the measurement reach experienced a greater rise). A more complex processing algorithm could recognize and correct for this error: A nonstreamflow-related variable is affecting *HR*.

[27] The channel of the Wabash River is wider than that of the Red River (Figure 3) and a larger bankfull discharge applies (approximately 2500 m^3/s). This river flows within a 10-km-wide floodplain inset below a gently rolling upland landscape (measured by the calibration pixel). The annual brightness temperature range is approximately 40°K for both measurement and calibration pixels; snow cover, crop cover, and soil moisture all may affect the brightness temperature values, with snow cover and snow melt being less important factors here than along the Red due to the Wabash location 18° to the south. During the recorded period, seven overbank floods occurred. Only the smallest one, in late June 2004, was not recorded by *HR*; this flow barely reached the bankfull stage and lasted only several days. There is only one spurious (but sub-bankfull) high flow indicated by *HR* (in February 2004; Figure 5). Sustained periods of low flow are well characterized for the Wabash River, as is the case also for the Red River.

[28] As commonly observed for stage-discharge ratings, individual river characteristics should influence rating equations based on reach surface water area, and this hinders the generalization of the approach to ungaged rivers without any local calibration [*Ashmore and Sauks*, 2006]. We consider also that the occurrence of lag times between peak stage and peak inundation may be a significant complicating factor for flood discharge measurement from remote sensing data. Figure 6 shows a portion of the Wabash results but without an incorporated lag. Peak inundation (peak *HR*), is reached approximately 2 days after the peak discharge and stage recorded at the gaging station. However, the shapes of the flood hydrographs are similar, and subaerial emergence of the floodplain is matched by gaging station-measured fall of river stage, again with a similar lag time. Such lags, as predicted by complex floodplain inundation dynamics [*Bates and Anderson*, 1996; *Bates et al.*, 1992, 1995, 1997; *Currey*, 1977; *Frappart et al.*, 2005; *Heiler et al.*, 1995; *Horitt and Bates*, 2001; *Hughes*, 1980; *Jung et al.*, 2004; *Magilligan*, 1988], should affect the daily *HR*-discharge scatterplots and the derived rating equations. As is the case for stage-discharge relations, hysteresis may be involved. These factors may reduce the amount of correlation exhibited in the scatterplots, and the precision of discharge estimation using rating equations based on such plots. However, the results for these two rivers demonstrate

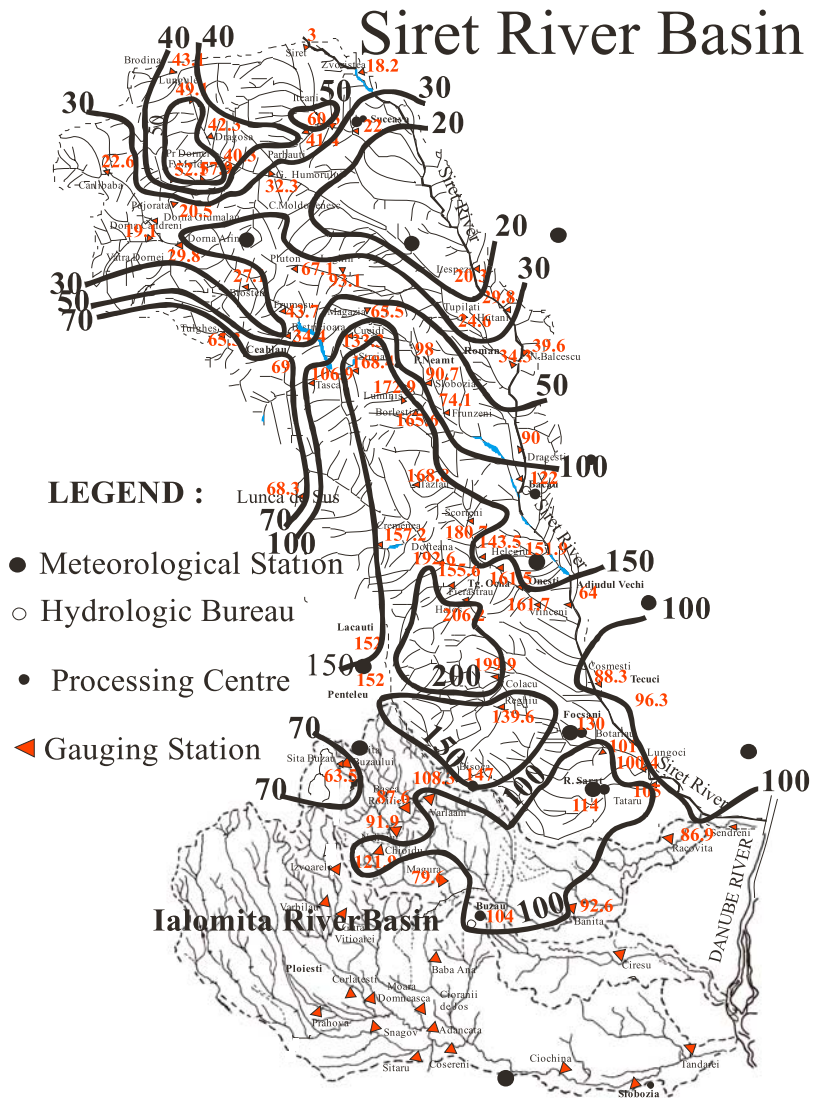

Figure 7. Isohyet map of precipitation during 10–14 July 2005 in the Siret River Basin, together with the local precipitation observations. The location of the Lungoci gaging station, also illustrated in Figure 3, is shown in the lower right portion of the map.

that even using a relatively low spatial resolution (but well calibrated) microwave sensor, it is possible to characterize with much temporal detail river discharge variation.

5. Measurement of a Flood Hydrograph Along the Siret River, Romania

[29] The Siret River (Figure 3) is a ~70-m-wide, sinuously meandering channel flowing within a broad floodplain. Small floods are constrained by artificial levees, but a large flood originating from very high rainfall (as high as 200 mm, 10–14 July 2005; Figure 7) inundated considerable portions of the floodplain. The flood was an extreme event (Figure 8) and caused at least 23 deaths and an estimated €1 billion in damage [*Brakenridge and Anderson*, 2006a]. Local gaging station daily discharge data for 2005 were used to calculate a third-order polynomial regression, $R^2 = 0.64$, of *HR* as the independent variable and Lungoci discharge as the dependent variable with a 2-day lag used in assigning dates to the Lungoci discharge. Figure 9 shows discharge estimated from the AMSR-E data and using this equation as the rating curve.

[30] AMSR-E data at the Siret gaging reach clearly detected and measured the flood hydrograph associated with this event (Figure 9). The remote sensing based flood hydrograph, with its very quick rise, is very similar to that recorded by the gaging station. In contrast, in-channel flow variability, before and after, is not detected by the paired measurement approach applied to these data (Figure 9). The channel is relatively narrow (~300 m) and the measurement pixel dimension (25 km) is relative large: We do not expect such small water area variations to be reliably recorded by the AMSR-E radiance values.

6. Calibration by Monthly Mean Discharge: African and Asian Examples

[31] For many regions of the world, daily discharge data are available only to authorized organizations within a nation and agency or ministry. In some cases, data sharing

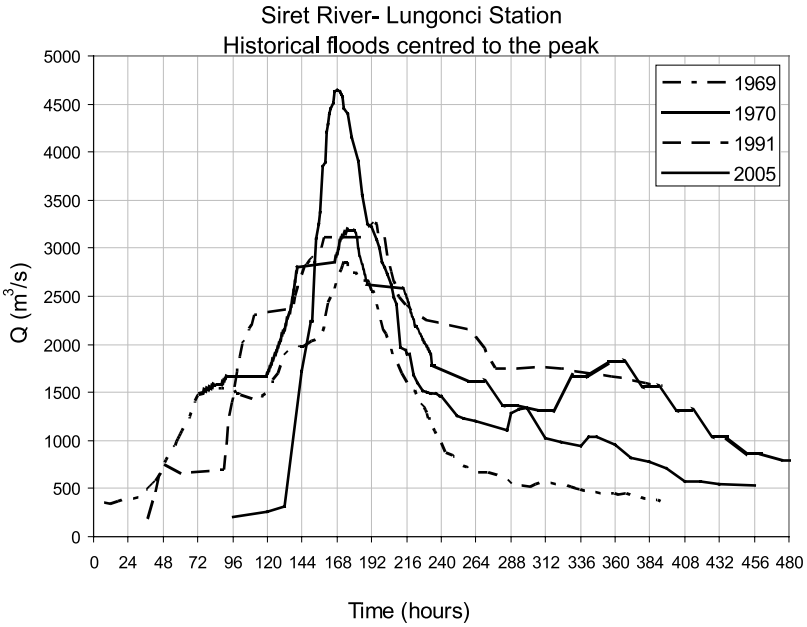

Figure 8. The 2005 flood hydrograph at Lungoci station compared with previous large floods in 1965, 1970, and 1971.

is not routinely accomplished even among different ministries. However, due in part to wide international participation in the World Meteorological Organization, monthly mean discharge data, for periods of several years up to several decades and mainly for the late twentieth century, are available: Global Runoff Data Center, http://grdc.bafg.de/servlet/is/Entry.987.Display/; http://www.sage.wisc.edu/riverdata/; http://www.rivdis.sr.unh.edu/.

[32] Such data are very useful for calibration of the AMSR-E time series at reaches where the remote sensing data can be colocated. Also, AMSR-E remote sensing may now be used to extend the record of each station up to the present and forward through time.

[33] The utility of this approach is demonstrated here. Figure 3 illustrates a selected gaging reach along the Niger River in Mali. Colocated to this reach is a gaging station at Dire (red triangle on the map in Figure 3). The published monthly mean discharge from this gaging station (1924–1992; http://www.rivdis.sr.unh.edu/) provides a record of long-term means along this strongly seasonal river. Monthly mean discharge ranges from 52 m^3/s in June to 1981 m^3/s in November. This large annual variation can be used to calibrate the AMSR-E record. Compilation of monthly mean values for *HR,* calculated from the paired AMSR-E brightness temperatures over mid-2002 through 2005, demonstrates a similar seasonal variation (Figure 10). Some uncertainty is introduced by the lack of temporal equiva-

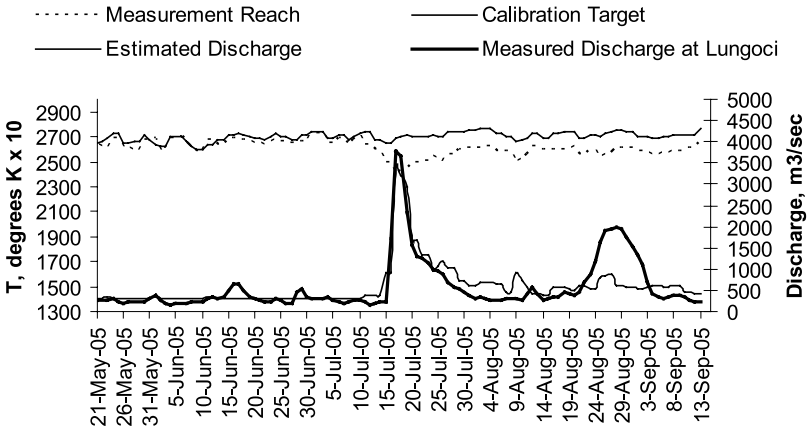

Figure 9. Remote sensing based discharge time series for Reach 268, along the Siret River, at Lungoci station and near Galati, eastern Romania. Upstream contributing area is 36,036 km^2. Detailed is the major flood in 2005, compared with gaging station discharge at Lungoci (discharge data provided by the Romanian Hydrological Administration, Bucharest).

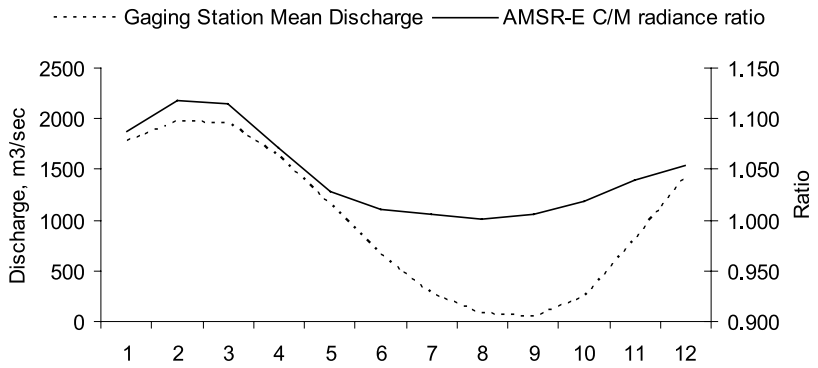

Figure 10. Monthly station discharge and *HR* values at Reach 433 for the Niger River, and Dire gaging station, Mali. Period of record for the monthly station data is 1924–1992, and the period of record for the *HR* time series is June 2002 to June 2006.

lence, but the two series are clearly correlated (see also Figure 11a). Such information offers a useful approach toward establishing an initial rating curve for inferring discharge from *HR*. It remains possible to further revise the rating curve if daily discharge values are eventually obtained for the appropriate time period. Figure 12, top plot, provides the resulting discharge time series using the AMSR-E *HR* discharge estimator as calibrated by the comparison of monthly means.

[34] The same strategy of comparing long-term monthly mean discharge data to mean values from remote sensing can be applied to many hundreds of sites, worldwide. Consistent measurements from now-defunct gaging stations can be extended, or current discharge status can be acquired for stations not otherwise sharing daily discharge information. Two more examples, from monsoonal Southeast Asia and from the seasonally ice covered Lena River in extreme northern Asia, further demonstrate the approach for river discharge measurement. Moreover, we also test the ability of AMSR-E to remotely detect river ice cover status.

[35] Figure 11b provides the rating curve based on monthly mean data for reach 77 along the Mekong River at Krachec in Cambodia, and Figure 12, middle plot, is the discharge reconstruction. According to the gaging station data, mean monthly discharge of the Mekong at this location varies from only 1808 m^3/s in April to 24,416 m^3/s in August, at the height of the monsoon. The data from AMSR-E can extend this information. Figure 12 shows that the seasonal rise and fall of the river can be quantitatively monitored, as is the case also for the Niger, and questions concerning the interannual variations, such as how soon in the year the river begins its rise and how long-lived is the enhanced runoff, can be addressed from these data.

[36] Figure 11c and Figure 12, lower plot, are the rating curve and the estimated discharge time series for the Lena River reach (see also Figure 3 for location map). Strong seasonality along the lower Lena is due to very long, cold winters separated by short but warm summers in which runoff is enhanced by snowmelt and permafrost thawing. Monthly mean discharge from a station farther downstream (at Stolb, Russia, not shown in Figure 3) provides in this case only crude calibration to actual discharge. However, at that station, monthly mean discharge in April, before ice cover removal, is 1734 m^3/s, and monthly discharge in June, at the peak of the annual flood, is 60,401 m^3/s. This seasonal variability is generally correlated to the monthly values of the AMSR-E data at the measurement reach (Figure 11). The preliminary rating curve can be constrained further by additional work (for example, by reducing discharge appropriately for the reduced known contributing area compared with that at Stolb). Also note that the rating equation for this reach (and for the others at high latitudes shown in Figure 2) substitutes a steady winter daily discharge once ice cover is established: as indicated through remote sensing by the autumn merging of the brightness temperatures values obtained for the two pixels (Figure 12).

[37] In this regard, for the Lena example, the time series of AMSR-E brightness temperatures, in blue (river measurement pixel) and green (calibration pixel), Figure 12, show the strong seasonal rhythm caused by temperature but also the effect of river ice conditions. During the summer, the measurement reach brightness temperature is much lower than the nearby calibration pixel because of the large surface water area provided by the open Lena River (Figure 3). Discharge variation during this season is sensitively tracked by the upwelling microwave radiance and *HR*. Once the river freezes in late October, the relative measurement and calibration brightness temperatures are reversed. Spring ice thaw and breakup are preceded by rises in radiance values at both. However, as documented by MODIS optical remote sensing data (Figure 13), in May, with river ice removal, the measurement pixel value drops very sharply and this change is not accompanied by similar changes at the calibration pixel (compare the bottom plot in Figure 12 with Figure 13). Thus an ice-cover algorithm for this river reach can be developed: When *HR* is negative, there is ice cover, and when it is positive, ice cover is not present.

7. Conclusion

[38] Contemporary orbital remote sensing with a high temporal resolution (daily or near-daily), as long used in the meteorological and oceanographic communities, is at a relatively low spatial resolution: 1 km to tens of kilometers. Such data have not commonly been used to measure localized terrestrial surface processes such as river discharge

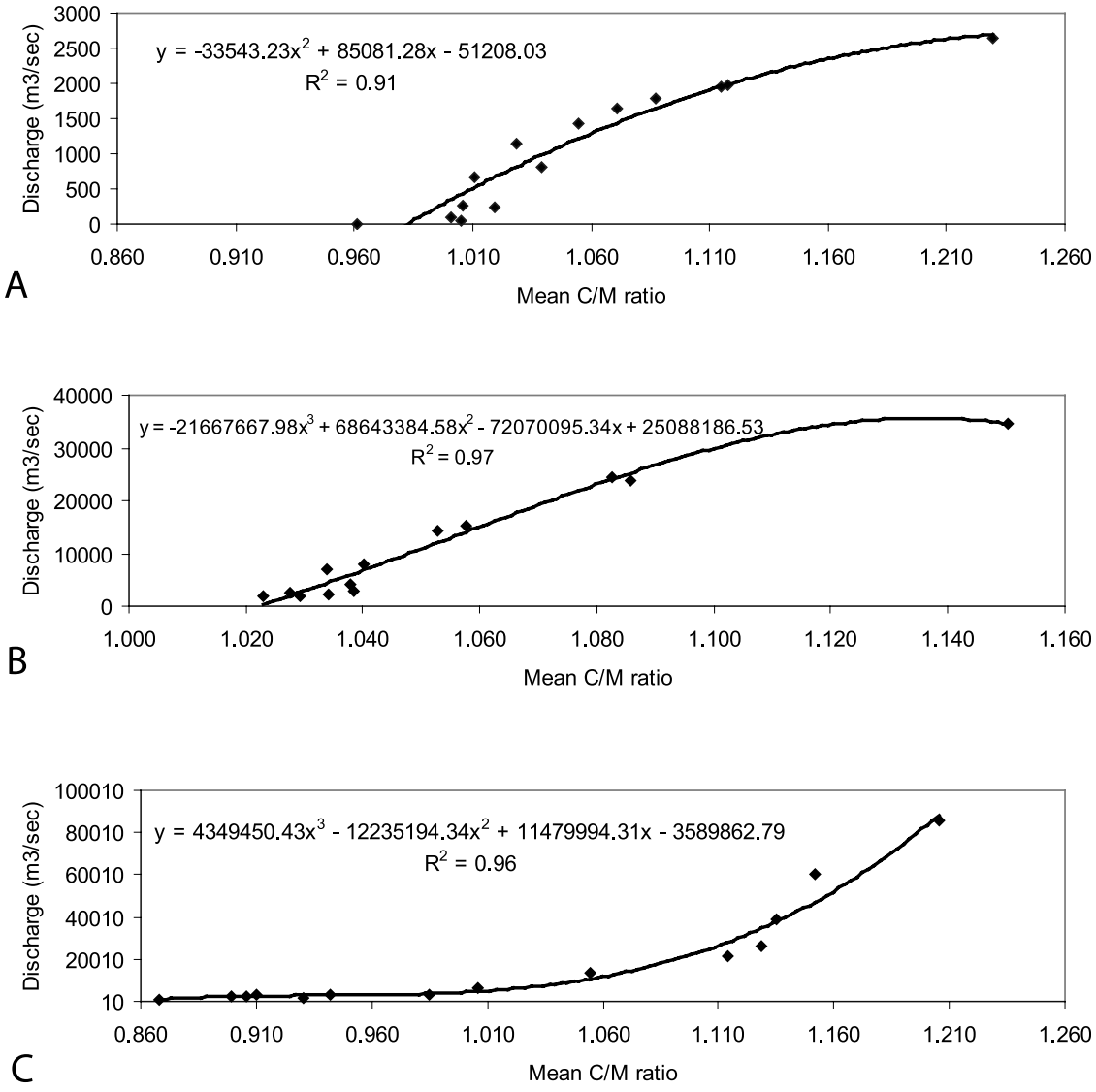

Figure 11. Scatterplots and rating curve equations comparing monthly mean *HR* values versus monthly mean gaging station discharges for three example reaches in Africa, southern Asia, and high-latitude Asia. (a) Niger reach at Timbuktu. An exponential equation is fit to the monthly data. *HR* values at and below 1.00 for this reach are assigned an estimated discharge of 0. (b) Reach 77, Mekong River, Krachech, Cambodia. A third-order polynomial equation defines the rating curve. (c) Reach 1, Lena River at Zhigansk, Siberia, Russia. A third-order polynomial equation defines the rating curve. Station data: Niger, Dire Station, Global Runoff Data Center 1134700, 1924–1002; Mekong, Pakse Station, Global Runoff Data Center 2469260, 1980–1993; Lena, Stolb Station, Global Runoff Data Center 2903430, 1978–1994, [*Fekete et al.*, 2000]. For the Lena, the rating equation applied in Figure 12 substitutes a steady winter discharge once ice cover is established and as indicated by the autumn merging of the brightness temperature (radiance) values of the calibration and measurement pixels.

and runoff. However, these processes are known to be highly dynamic: Floods may have durations of only hours or a few days, and spring floods in cold regions as well as monsoonal flooding in lower latitudes cause stream flow variation over several orders of magnitude and over large areas. In particular, the dynamic nature and the geographic extent of rivers pose severe problems for characterization via terrestrial remote sensing satellites such as Landsat or Radarsat, which cannot provide frequent revisits or wide-area coverage. Instead, surface water monitoring requires an observational capability that can track changes quickly and frequently over large geographic areas, even though such changes are expressed on a spatially restricted basis within those areas.

[39] The paired measurement approach was developed in order to meet this challenge, and to enhance the capability to measure and characterize a critical component of the Earth's water cycle: surface water runoff. Microwave remote

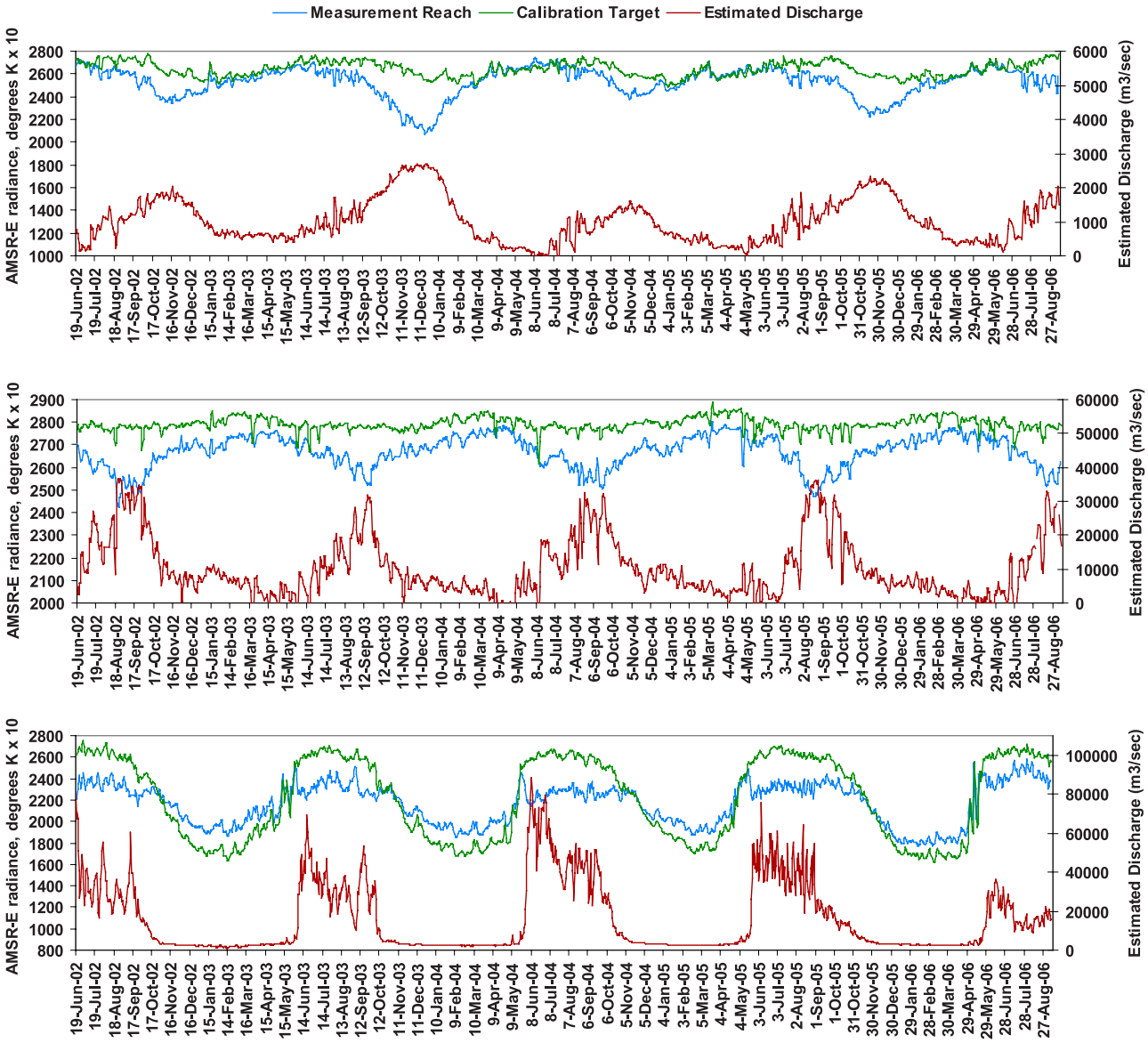

Figure 12. AMSR-E radiance data (left axis scale) for the measurement (blue line) and calibration (green line) pixels, and estimated discharge (brown line, right axis scale), using the rating curves provided in Figure 11, for (top) Reach 433 along the Niger River; (middle), Reach 77 along the Mekong River; and (bottom) Reach 1 along the Lena River.

sensing is an attractive approach because frequencies can be chosen such that the microwave signatures are not obscured by cloud cover or solar illumination. As noted, predictable sampling in time is crucial for monitoring runoff. The work presented here indicates that AMSR-E microwave measurements at a frequency of 36.5 GHz, horizontal polarization, descending orbit (night overpass) data, calibrated via the paired measurement approach, and obtained over carefully selected river reaches, can characterize river discharge changes at a useful level of accuracy. Calibration to discharge of the remote sensing signal is made possible by ground-based discharge information, even if such are limited to monthly means. Such space-based data can have broad utility in the hydrological sciences due to the global geographic coverage. The presence of river ice cover can also be detected, and the timing of ice freeze-up and ice removal can be determined for many river reach locations in cold land regions. It is now possible to measure the length and magnitudes of monsoon-driven high water in south Asia and other locations on a consistent basis over large areas. Moreover, because it is surface water areal extent that is actually sensed, there is a clear potential for sustained monitoring of ecologically important wetlands. The technique can be applied regionally, with a relatively dense sampling networks, or globally, with a relatively sparse sampling network focused on, for example, critical flood hazard locations or on capturing the greatest proportion of total freshwater runoff entering the oceans.

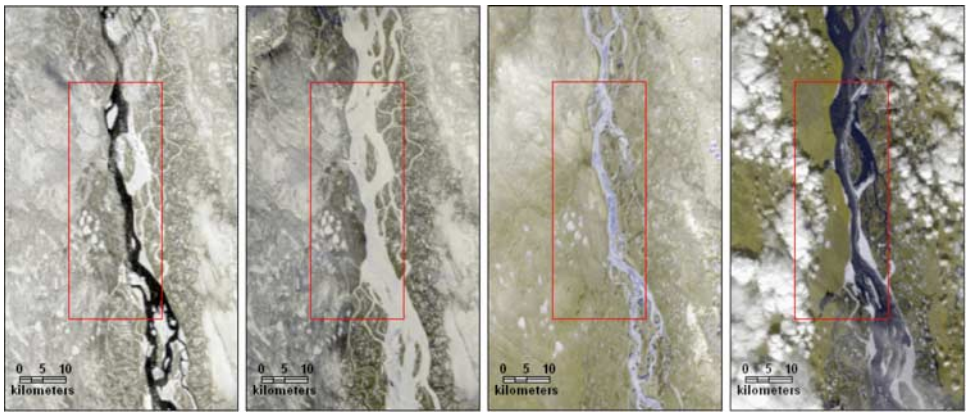

Figure 13. MODIS optical imaging of Reach 1, Lena River at Zhigansk. From left to right: 11 October 2002 and 6 November 2002, as an example of the ice freeze-up process, and 28 May 2003 and 6 June 2003 as an example of the ice breakup process. Compare with the plots in Figure 12, bottom. The red square is the measurement pixel.

[40] This paper presents a new technology and the rudiments of a methodology for measuring river discharge. However, much remains to be done to transition this capability into the routine and accurate measurements that are needed. The scatterplots/rating curves comparing the remote sensing estimator (*HR*) to discharge measured by ground stations demonstrate robust covariance, but they also imply that discharge accuracy and precision will be different for low flow, for in-channel flow variation, and for large floods. A satisfactory analysis of error will likely produce different confidence intervals for different portions of the flow regime; such analysis remains to be accomplished. Computation of monthly runoff volumes, obtained by summing daily volumes inferred from daily *HR* values, also reduces measurement errors significantly. Finally, large flood discharges are commonly not well measured even by ground gaging stations: The stations may be destroyed by floods, or the flood stage may exceed the rating curves, or the flood may alter the rating curve by modifying the channel and floodplain geometry. Thus, as is the case for in situ station data, the remote sensing *HR* values may define a new flood's magnitude ranking within the flow series accurately, but obtaining an accurate peak discharge for the event may require additional information, such as velocity measurements and ground-based surveys.

[41] The possible applications of this new approach to surface hydrology measurements include studies of global- or regional-scale runoff, investigations of effects of river plumes on physical and ecological characteristics in coastal oceans, and early and consistent detection of floodplain inundation for national and international disaster response purposes. If performed at upstream locations in real time, such remote sensing could also provide flood warnings to affected populations. Drought can also be quantified in this observational approach in a manner complementary to other indicators. For example, in some regions of Africa, drought is caused by severe reductions in seasonal rainfall and river runoff. In this and other regions, where gaging networks have largely been lost, river monitoring networks with satellite data can now be designed to replace such critical information.

[42] **Acknowledgments.** The research carried out at the Jet Propulsion Laboratory, California Institute of Technology was supported under a contract with NASA, and that at Dartmouth College was supported by NASA and by the North Atlantic Treaty Organization (NATO) Science for Peace Programme.

References

Anderson, M. G., et al. (1996), The general context of floodplain process research, in *Floodplain Processes*, edited by M. G. Anderson et al., pp. 1–13, John Wiley, Hoboken, N. J.

Ashmore, P., and E. Sauks (2006), Prediction of discharge from water surface width in a braided river with implications for at-a-station hydraulic geometry, *Water Resour. Res.*, *42*, W03406, doi:10.1029/2005WR003993.

Bates, P. D., and M. G. Anderson (1996), A preliminary investigation into the impact of initial conditions on flood inundation predictions using a time/space distributed sensitivity analysis, *Catena*, *26*, 115–134.

Bates, P. D., et al. (1992), Modeling floodplain flow with a two-dimensional finite element scheme, *Earth Surf. Processes Landforms*, *17*, 575–588.

Bates, P. D., et al. (1995), Initial comparison of two two-dimensional finite element codes for river flood simulation, *Proc. Inst. Civ. Eng. Water Mar. Energy*, *112*, 238–248.

Bates, P. D., et al. (1997), Integrating remote sensing observations of flood hydrology and hydraulic modeling, *Hydrol. Processes*, *11*, 1777–1795.

Bates, P. D., et al. (2002), Optimal use of high-resolution topographic data in flood inundation models, *Hydrol. Processes*, *17*, 537–557.

Bayley, P. B. (1991), The flood pulse advantage and the restoration of large river-floodplain systems, *Reg. Rivers Res. Manage.*, *6*, 75–86.

Bjerklie, D. M., et al. (2003), Evaluating the potential for measuring river discharge from space, *J. Hydrol.*, *278*, 17–38.

Brakenridge, G. R., and E. Anderson (2006a), Active archive of large floods, 1985–Present, Dartmouth Flood Obs, Dartmouth Coll., Hanover, N. H. (Available at http://www.dartmouth.edu/%7Efloods/Archives/index.html)

Brakenridge, G. R., and E. Anderson (2006b), World atlas of flooded lands, Dartmouth Flood Obs, Dartmouth Coll., Hanover, N. H. (Available at http://www.dartmouth.edu/~floods/Atlas.html)

Brakenridge, G. R., et al. (2002), Satellite gaging reaches: A strategy for MODIS-based river monitoring, paper presented at the 9th International Symposium on Remote Sensing, Int. Soc. for Opt. Eng., Crete, Greece, 22 –27 Sept.

Brakenridge, G. R., S. V. Nghiem, E. Anderson, and S. Chien (2005), Space-based measurement of river runoff, *Eos Trans. AGU*, *86*(19), 185–188.

Calvet, J.-C., et al. (1995), Microwave dielectric properties of a silt-loam at high frequencies, *IEEE Trans. Geosci. Remote Sens.*, *33*, 634–642.

Currey, D. T. (1977), Identifying flood water movement, *Remote Sens. Environ.*, *6*, 51–61.

Fairbridge, R. W., and C. W. Finkl (1979), *The Encyclopedia of Soil Science: Part 1, Physics, Chemistry, Biology, Fertility, and Technology*, *Encycl. Earth Sci.*, vol. XII, edited by R. W. Fairbridge and C. W. Finkl Jr., Van Nostrand Reinhold, Hoboken, N. J.

Fekete, B. M., C. J. Vörösmarty, and W. Grabs (2000), UNH/GRDC composite runoff fields, V 1.0, Univ. of N. H., Durham. (Available at http://www.grdc.sr.unh.edu/)

Frappart, F., et al. (2005), Floodplain water storage in the Negro River basin estimated from microwave remote sensing of inundation are and water levels, *Remote Sens. Environ.*, *99*, 387–399.

Heiler, H., et al. (1995), Hydrological connectivity and flood pulses as the central aspects for the integrity of a river-floodplain system, *Regul. Rivers*, *11*, 351–361.

Horitt, M. S., and P. D. Bates (2001), Predicting flood plain inundation: Raster based modeling versus the finite element approach, *Hydrol. Processes*, *15*, 825–842.

Hughes, D. A. (1980), Floodplain inundation: Processes and relationships with channel discharges, *Earth Surf. Processes*, *5*, 297–304.

Jung, M., T. P. Burt, and P. D. Bates (2004), Toward a conceptual model of floodplain water table response, *Water Resour. Res.*, *40*, W12409, doi:10.1029/2003WR002619.

Klein, L. A., and C. T. Swift (1977), Improved model for dielectric-constant of sea-water at microwave-frequencies, *IEEE Trans. Antennas Propag.*, *25*, 104–111.

Magilligan, F. J. (1988), Variations in slope components during large magnitude floods, Wisconsin, *Ann. Assoc. Am. Geogr.*, *78*, 520–533.

Mertes, K. A. K. (1997), Documentation and significance of the perirheic zone on inundated floodplains, *Water Resour. Res.*, *33*, 1749–1762.

Nghiem, S. V., et al. (1990), Polarimetric remote sensing of geophysical media with layer random medium model, in *Progress in Electromagnetics Research*, vol. 3, edited by J. A. Kong, pp. 1–73, Elsevier, New York.

Njoku, E. G., et al. (2003), Soil moisture retrieval from AMSR-E, *IEEE Trans. Geosci. Remote Sens.*, *41*, 215–229.

Njoku, E. G., et al. (2005), Global survey and statistics of radio-frequency interference in AMSR-E land observations, *IEEE Trans. Geosci. Remote Sens.*, *43*, 938–947.

Rantz, S. E., et al. (1982), *Measurement and Computation of Streamflow*, vol. 1, *Measurement of Stage and Discharge*, *U. S. Geol. Surv. Water Supply Pap.*, *2175*, 80–82.

Skou, N. (1989), *Microwave Radiometer Systems: Design and Analysis*, Artech House, Norwood, Mass.

Smith, L. C. (1997), Satellite remote sensing of river inundation area, stage, and discharge: A review, *Hydrol. Processes*, *11*, 1427–1439.

Smith, L. C., et al. (1995), Estimation of discharge from braided glacial rivers using ERS 1 synthetic aperture radar: First results, *Water Resour. Res.*, *31*, 1325–1329.

Smith, L. C., et al. (1996), Estimation of discharge from three braided rivers using synthetic aperture radar satellite imagery, *Water Resour. Res.*, *32*, 2021–2034.

Tsang, L. (1991), Polarimetric passive remote sensing of random discrete scatterers and rough surfaces, *J. Electromagn. Waves Appl.*, *5*, 41–57.

Tsang, L., et al. (1985), *Theory of Microwave Remote Sensing*, John Wiley, Hoboken, N. J.

Wahl, K. L., et al. (1995), Stream-gaging program of the U. S. Geological Survey, *U. S. Geol. Surv. Circ.*, *1123*.

Yueh, S. H., et al. (1992), Polarimetric emission from anisotropic media with its applications for passive remote sensing of sea ice, paper presented at 12th Annual International Geophysics and Remote Sensing Symposium, Int. of Electr. and Electr. Eng., Houston, Tex.

E. Anderson and G. R. Brakenridge, Dartmouth Flood Observatory, Department of Geography, Dartmouth College, Hanover, NH 03755, USA. (robert.brakenridge@ dartmouth.edu)

R. Mic, National Institute of Hydrology and Water Management, Bucharest 031686, Romania. (rodica.mic@hidro.ro)

S. V. Nghiem, Jet Propulsion Laboratory, California Institute of Technology, 4800 Oak Grove Drive, MS 300-235, Pasadena, CA 91109, USA. (son.v.nghiem@jpl.nasa.gov)